Dalton Transactions

PAPER

View Article Online
View Journal | View Issue

Check for updates

Cite this: *Dalton Trans.*, 2018, **47**, 1498

Effect of linear and non-linear pseudohalides on the structural and magnetic properties of Co(II) hexacoordinate single-molecule magnets†

L. Váhovská,[a,b] S. Vitushkina,[c] I. Potočňák,[b] Z. Trávníček [d] and R. Herchel *[d]

Received 10th November 2017,
Accepted 15th December 2017

DOI: 10.1039/c7dt04256f

rsc.li/dalton

A series of mononuclear hexacoordinate Co(II) complexes with the 4-amino-3,5-bis(2-pyridyl)-1,2,4-triazole (abpt) ligand and various linear and non-linear pseudohalides, such as NCSe (selenocyanate), N{C(CN)$_2$}$_2$ (1,1,3,3-tetracyano-2-azapropenide, tcap), NO$_2$C(CN)$_2$ (nitrodicyanomethanide, nodcm), C(CN){C(CN)$_2$}$_2$ (1,1,2,3,3-pentacyanopropenide, pcp), NO$_2$NCN (nitrocyanamide, nca), and ONC(CN)$_2$ (nitrosodicyanomethanide, ndcm), was prepared. X-ray analyses revealed the formation of the complexes with the general compositions [Co(abpt)$_2$(solv)$_2$]X$_2$ (solv = H$_2$O and X = tcap (**1**), solv = H$_2$O and X = nodcm (**2**), solv = CH$_3$OH and X = pcp (**3**)) or [Co(abpt)$_2$(X)$_2$] (X = nca (**4**), X = NCSe (**5**), X = ndcm (**6**)). The impact of axial co-ligands (solv or X) on the magnetic properties was investigated experimentally by measuring temperature- and field-dependent static (DC) and dynamic magnetic (AC) data as well as theoretically using the CASSCF/NEVPT2, AILFT, and AOM methods. Large magnetic anisotropy was found for all complexes **1–6** and was treated either by the spin Hamiltonian or with the Hamiltonian including the orbital angular momentum. Furthermore, the AC susceptibility measurements confirmed the slow relaxation of the magnetization in a non-zero static magnetic field, thus these complexes can be classified as field-induced single-molecule magnets with an estimated energy barrier U_{eff} up to 100 K.

Introduction

The mononuclear cobalt(II) coordination compounds have attracted a lot of interest since the discovery of so-called single-ion magnets (SIMs),[1] which form a subclass of the large family of single-molecule magnets (SMMs) having only one paramagnetic metal ion within the complex unit. The characteristic feature of SMMs is slow relaxation of the magnetization and magnetic hysteresis at low temperatures originating at the molecular level.[2,3] Thus, these molecular nanomagnets are fascinating molecular materials due to their auspicious application potential in, for example, information storage, quantum computing, and spintronics.[4]

The magnetic bistability of SMMs is due to the existence of the energy barrier (U) acting against the spin momentum reversal. In the case of 3d-metal complexes, U is usually related to the zero-field splitting (ZFS)[5] of the ground spin state as $U = |D|S^2$ for an integer and $U = |D|(S^2 - 1/4)$ for a non-integer spin value S, where D is the axial ZFS parameter defined within the spin Hamiltonian formalism. The advantage of SIMs is that the magnetic anisotropy of mononuclear complexes can be tuned by the rational design of the ligand field strength of the utilized ligands and their coordination geometry around the central atom.[6] This contrasts with polynuclear SMMs, in which it is hard to predict the ground state properties due to variation of the exchange coupling among metal atoms and their overall contributions to the magnetic anisotropy. Furthermore, it was shown that increasing the number of metal atoms in polynuclear compounds does not explicitly lead to an increase of U due to the mutual relation between S and D.[7] To date, many SIMs have been reported for 3d-metals with various coordination numbers and geometries, *e.g.* Fe(I^8/II^9/III^{10}), Ni(I^{11}/II^{12}), Cu(II),[13] or Mn(III).[14] The history of mononuclear Co(II) compounds exhibiting slow relaxation of magnetization started in 2011,[15] and was followed by further reports on SMM behavior in tetra-,[16] penta-,[17] hexa-,[18]

[a]*P. J. Šafarik University in Košice, Department of Inorganic Chemistry, Institute of Chemistry, Moyzesova 11, Košice, Slovakia*
[b]*University of Veterinary Medicine and Pharmacy in Košice, Department of Chemistry, Biochemistry and Biophysics, Institute of Biochemistry, Komenského 73, Košice, Slovakia*
[c]*V.N. Karazin Kharkov National University, Faculty of Chemistry, Department of Applied Chemistry, Svobody sq. 4, Kharkov, Ukraine*
[d]*Department of Inorganic Chemistry, Regional Centre of Advanced Technologies and Materials, Faculty of Science, Palacký University, 17. listopadu 12, Olomouc, Czech Republic. E-mail: radovan.herchel@upol.cz*

†Electronic supplementary information (ESI) available: Additional X-ray data, magnetic data and analysis, and details of theoretical calculations. CCDC 1583578–1583583. For ESI and crystallographic data in CIF or other electronic format see DOI: 10.1039/C7DT04256F

Open Access Article. Published on 19 December 2017. Downloaded on 9/21/2024 9:05:42 PM.
This article is licensed under a Creative Commons Attribution-NonCommercial 3.0 Unported Licence.

This journal is © The Royal Society of Chemistry 2018

Open Access Article. Published on 19 December 2017. Downloaded on 9/21/2024 9:05:42 PM.
This article is licensed under a Creative Commons Attribution-NonCommercial 3.0 Unported Licence.

hepta-,[19] or octa-coordinate[20] mononuclear Co(II) coordination compounds.

In the case of hexacoordinate Co(II) complexes, two limiting geometries can be distinguished, either an ideal octahedron or trigonal prism, both possessing an orbitally degenerate ground state, *i.e.* either $^4T_{1g}$ for O_h or ^4E for D_{3h}. This can lead to a huge magnetic anisotropy and hence large U. However, until now, the slow relaxation of magnetization in a zero static magnetic field has only been reported for geometries close to D_{3h}.[21,22] In the case of (pseudo)octahedral complexes, the deviation from the ideal geometry to D_{4h} symmetry can lead again to the orbitally degenerate ground state ^4E_g for an elongated tetragonal bipyramid or to the $^4A_{2g}$ ground state for a compressed tetragonal bipyramid. Such geometrical changes accompanied by variation in the ligand field strength and donor atoms' properties can result in easy-axis/easy-plane magnetic anisotropy or even in triaxial magnetic anisotropy. This richness of conceivable magnetic behavior is inspiring for a deeper study of hexacoordinate Co(II) complexes as candidates for SIMs.

Recently, we have reported on a hexacoordinate $[Co(abpt)_2(tcm)_2]$ compound (abpt = 4-amino-3,5-bis(2-pyridyl)-1,2,4-triazole, tcm = $C(CN)_3$, tricyanomethanide) behaving as a field-induced SIM with positive axial ($D > 0$) and large rhombic anisotropy ($E/D \gg 0$).[23] This motivated us to prepare and study a series of novel mononuclear hexacoordinate Co(II) compounds utilizing the bidentate abpt ligand with other linear and non-linear pseudohalides, such as NCSe (selenocyanate), $N\{C(CN)_2\}_2$ (1,1,3,3-tetracyano-2-azapropenide, tcap), $NO_2C(CN)_2$ (nitrodicyanomethanide, nodcm), $C(CN)\{C(CN)_2\}_2$ (1,1,2,3,3-pentacyanopropenide, pcp), NO_2NCN (nitrocyanamide, nca), and $ONC(CN)_2$ (nitrosodicyanomethanide, ndcm). In this paper, we report their molecular/crystal structures, static and dynamic magnetic properties, and theoretical calculations at the CASSCF/NEVPT2 level, which were employed to better understand their magnetic features.

Results and discussion

Syntheses and characterization

In order to obtain analogous compounds with a similar composition to the $[Co(abpt)_2(tcm)_2]$ compound described earlier,[23] we performed several syntheses with the above-mentioned pseudohalide anions. A stoichiometric reaction between cobalt(II) chloride, abpt, and appropriate non-linear pseudohalide anions in a water–methanol solution gave three ionic mononuclear complexes **1–3** with the general composition $[Co(abpt)_2(solv)_2]X_2$, where solv = H_2O (**1** and **2**) or CH_3OH (**3**) and X = tcap (**1**), nodcm (**2**), and pcp (**3**), and one molecular complex with the composition $[Co(abpt)_2(X)_2]$ (X = nca) (**4**). Thus, the same synthetic procedure led to two different types of octahedral complex, probably due to the different steric hindrance of the respective non-linear pseudohalide anions. Although the bulky anions in **1–3** could not enter the Co(II) coordination sphere and therefore solvent molecules must coordinate, the smaller nca anion in **4** could coordinate as the ligand (Scheme 1).

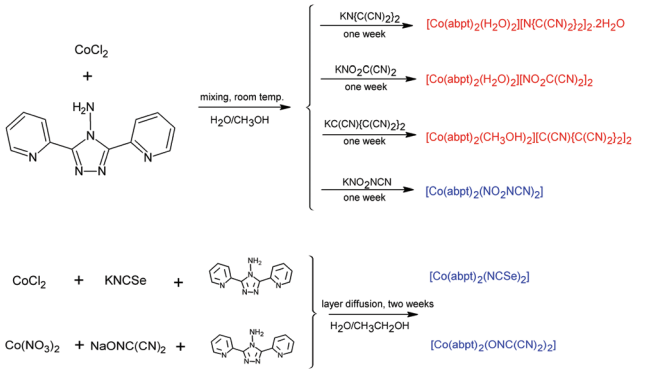

Scheme 1 Schematic representations of the synthetic procedures leading to the preparation of **1–6**. Ionic complexes are written in red, while molecular complexes are written in blue.

Attempts to prepare analogous $[Co(abpt)_2(X)_2]$ molecular complexes with NCSe (**5**) and ndcm anions (**6**) using the same synthetic procedure as that used in the case of **1–4** were not successful and only powder products were obtained. Elemental analyses indicated the $[Co(abpt)_2(X)_2]$ (X = NCSe or ndcm) composition, thus we prepared their single crystals using diffusion of the corresponding reactants in a 1 : 1 : 1 molar ratio.

The IR spectra of the prepared complexes are quite similar. The presence of the abpt ligand was confirmed by the following characteristic vibrations: ν(N–H) vibrations of the amino group were located in the 3250–3140 cm^{-1} region; $\nu(C–H)_{ar}$ vibrations were found in the 3080–3015 cm^{-1} region; and $\nu(C{=}C)_{ar}$ and $\nu(C{=}N)_{ar}$ bands were observed in the 1635–1500 cm^{-1} and 1500–1400 cm^{-1} regions, respectively.[24] The shifts of those bands to higher wavenumbers with respect to the IR spectrum of free abpt clearly suggest the coordination of the abpt ligand in all of the prepared compounds. The main spectral variations of complexes **1–6** compared to those of free abpt are found in the 408–415 cm^{-1} (out-of-plane ring deformation) and 604–612 cm^{-1} (in-plane ring deformation) regions, where absorptions of the pyridine ring of the abpt ligand occur.[25] These vibrations in **1–6** are found to be positively shifted, suggesting the coordination of the pyridine nitrogen atom to the metal atom.[26] In the spectra of **1–3**, bands connected with the vibrations of water or methanol molecules were also observed.

Bands for $\nu(C{\equiv}N)$ stretching vibrations from the pseudohalide anions in **1–3**, observed in the 2227–2191 cm^{-1} region, show similar patterns to those for their corresponding free potassium salts K(tcap) for **1**, K(nodcm) for **2**, and K(pcp) for **3** (2230–2190 cm^{-1}).

Similar wavenumbers and numbers of the absorption bands suggest the presence of uncoordinated polynitrile CN groups as was confirmed by the X-ray structures (*vide infra*). However, two strong split bands at 2220 and 2002 cm^{-1} were observed in the spectrum of **2**, while only one band at 2210 cm^{-1} was observed in the spectrum of free K(nodcm).

Open Access Article. Published on 19 December 2017. Downloaded on 9/21/2024 9:05:42 PM.
This article is licensed under a Creative Commons Attribution-NonCommercial 3.0 Unported Licence.

The higher number of bands in the spectrum of **2** indicates a non-equivalence of both terminal cyano groups due to the different number of hydrogen bonds in which both cyano groups are involved. On the other hand, for **4** and **5**, only one strong band at 2204 cm^{-1} and 2083 cm^{-1} respectively is observed and is significantly shifted to higher wavenumbers compared with the bands observed for the free K(nca) (2188 cm^{-1}) and KNCSe (2064 cm^{-1}), respectively, suggesting coordination of the cyano group to the central atom. Unlike that in the IR spectrum of the free Na(ndcm), the one very strong ν(C≡N) stretching vibration is split into two medium peaks around 2218 and 2212 cm^{-1} in the spectrum of **6**. This splitting can be explained by the non-equivalence of the nitrile groups, because only one of them is involved in the intermolecular hydrogen bonding (Fig. S6†).

Description of structures 1–3

The unit cell parameters and crystal and refinement data for $[Co(abpt)_2(H_2O)_2](N\{C(CN)_2\}_2)_2\cdot 2H_2O$ (**1**), $[Co(abpt)_2(H_2O)_2](NO_2C(CN)_2)_2$ (**2**), and $[Co(abpt)_2(CH_3OH)_2](C(CN)\{C(CN)_2\}_2)_2$ (**3**) are summarized in Table S1.† In each structure, the asymmetric unit consists of a cobalt atom on an inversion center, one abpt and one water or methanol molecule coordinated to the cobalt, and one uncoordinated pseudohalide anion (Fig. 1). Thus, the Co(II) central atom adopts a CoN_4O_2 distorted octahedral geometry with four equatorial N atoms from two abpt chelating ligands and two axial O atoms from the coordinated molecules of the solvents. Selected bond lengths and angles for the cobalt coordination sphere are summarized in Table 1 and Table S2.†

The averaged Co–N bond distances involving the pyridyl groups [Co1–N50 = 2.154(10) Å] are larger than those corresponding to the triazole rings [Co1–N10 = 2.084(27) Å], which is in good agreement with other coordination compounds containing the abpt ligand.[27] The axial Co–O bond distances in **1–3** are found in the range of 2.102(1)–2.118(2) Å. The averaged bite angle N10–Co1–N50 (76.88(18)°) strongly differs from 90° as expected for atoms coordinated in the *cis* position. The abpt ligand is nearly planar with dihedral angles between the triazole and coordinated or uncoordinated rings near to 3.7° and 10.8° on average, respectively. Moreover, the nitrogen atom of the uncoordinated pyridyl ring is projected to the amine group of the triazole ring due to the presence of an intramolecular hydrogen bond, which contributes to the almost planar configuration of the abpt ligand. These facts have been reported in most of the previously described coordination compounds with this ligand.[27]

Table 1 Selected donor–acceptor bond lengths (Å) and the octahedral deformation parameter Σ (°) in the crystal structures of **1–6**[a]

	d(Co-N_{tr})	d(Co-N_{py})	d(Co-O_{ax}/N_{ax})	Σ
1	2.081(1)	2.166(1)	2.102(1)	60.0
2	2.112(2)	2.146(2)	2.118(2)	53.2
3	2.058(1)	2.151(1)	2.109(1)	65.4
4	2.086(2)	2.144(2)	2.121(2)	53.2
5	2.086(3)	2.165(2)	2.121(3)	66.3
6	2.104(2)	2.142(2)	2.092(1)	76.4

[a] Octahedral distortion calculated as $\Sigma = \sum_{i=1}^{12} |90 - \alpha_i|$, where α_i stands for 12 *cis* angles of the coordination polyhedron.

The tcap, nodcm, and pcp pseudohalide anions are nearly planar too, with the largest deviation of atoms from the mean planes being 0.048(1) for N2, 0.074(2) for O2, and 0.265(2) Å for atom N5. Due to the presence of the supplementary π-electron systems of the cyano groups in the pseudohalide anions, strong electronic delocalization is observed, as indicated by a number of almost equivalent C–C bond lengths, in the range of 1.433(2)–1.438(2) in **1**, 1.407(3)–1.418(3) in **2**, and 1.378(3)–1.477(2) Å in **3**, which are shorter than typical single C–C bonds (1.54 Å). This delocalization also includes the C=N bonds in **1** and **2**, which are slightly longer than double C=N bonds (1.27 Å).[28] All $N_{cyanide}$≡C distances (1.148(4) Å on average) are close to triple N≡C bond distances (1.15 Å) (Table S2†).

The crystal packing is very compact because of short face-to-face distances (Table S5†) and strong O–H···N, O–H···O, and N–H···O intermolecular hydrogen bonds (Table S4†). Due to these hydrogen bonds, a two-dimensional supramolecular layer in the *ab* plane in **1** (Fig. S1†), a three-dimensional supramolecular network in **2** (Fig. S2†), and a one-dimensional chain parallel to the [0$\bar{1}$1] direction in **3** (Fig. S3†) are formed. Moreover, in all the discussed complexes, the amino group of

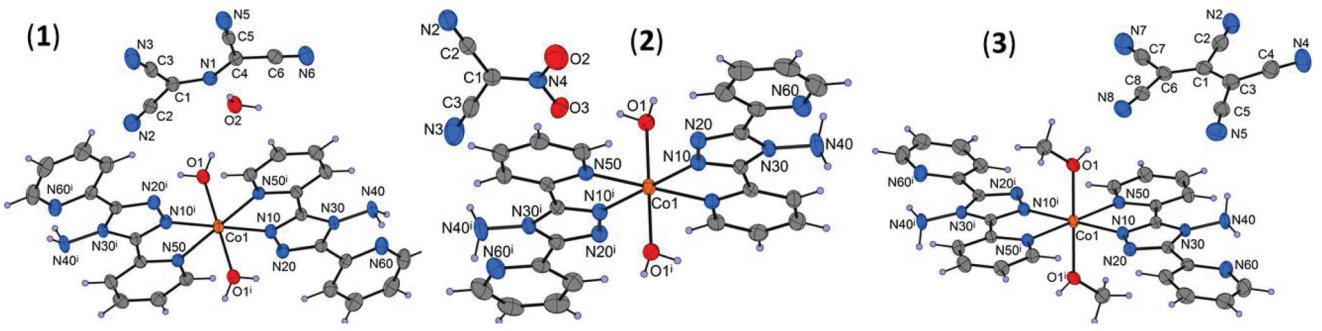

Fig. 1 Molecular structures of **1–3** with displacement ellipsoids (50% probability). [Symmetry codes: (i) 1 – *x*, 1 – *y*, 1 – *z* (**1**) and (i) 1 – *x*, 1 – *y*, –*z* (**2** and **3**)].

 This journal is © The Royal Society of Chemistry 2018

Open Access Article. Published on 19 December 2017. Downloaded on 9/21/2024 9:05:42 PM.
This article is licensed under a Creative Commons Attribution-NonCommercial 3.0 Unported Licence.

abpt is involved in the intramolecular hydrogen bond linking the uncoordinated pyridyl and triazole rings of abpt. π–π interactions are present between uncoordinated pyridyl rings (containing N60 atoms) of the abpt ligands from the neighboring complexes, with an averaged centroid–centroid distance of 3.79(9) Å. The π–π stacking interactions between the abpt ligands link the 2D hydrogen-bonded layers in **1** and 1D hydrogen-bonded chains in **3** and lead to supramolecular 3D structures, while in **2** π–π stacking interactions contribute to the higher stabilization of the crystal structure.

Description of structures 4–6

The $[Co(abpt)_2(NO_2NCN)_2]$ (**4**), $[Co(abpt)_2(NCSe)_2]$ (**5**), and $[Co(abpt)_2\{ONC(CN)_2\}_2]$ (**6**) complexes have a similar structure to that previously described for $[Co(abpt)_2(tcm)_2]$.[23] The molecular structures of **4–6** consist of discrete $[Co(abpt)_2X_2]$ complexes, where two equivalent chelating abpt ligands stand in the equatorial plane and two equivalent terminal pseudohalide ligands (X) complete the coordination sphere in the *trans* positions (Fig. 2). Similar *trans* coordination of the two pseudohalide ligands was observed in the isostructural $[M(abpt)_2(X)_2]$ complexes with M = Fe (X = NCS,[29] NCSe,[30] $C(CN)_3$, $(NC)_2CC(OCH_3)C(CN)_2$, $(NC)_2CC(OC_2H_5)C(CN)_2$,[31] $N(CN)_2$,[32]), M = Ni ($X = N_3$),[33] and M = Co (X = NCS).[34] Only half of the complex is present in the asymmetric unit of **4–6**; the second half is generated by a center of inversion located at the cobalt(II) atom. Each Co(II) atom is in a distorted $[CoN_6]$ (**4** and **5**) or $[CoN_4O_2]$ (**6**) octahedral environment; selected bond lengths and bond angles are summarized in Table 1 and Table S3.†

As in **1–3**, the $Co–N_{pyridyl}$ bond distances (Co1–N50 = 2.150(13) Å on average) are longer than those involving the triazole rings (Co1–N10 = 2.092(10) Å on average) and the pseudohalide groups (Co1–X1 = 2.111(17) Å on average, X = N (**4** and **5**) or O (**6**)). The deformed octahedral geometry around Co1 in **4–6** is demonstrated mainly by the values of the N10–Co1–N50 bite angles (Table S3†), which strongly differ from the ideal 90° value for *cis* coordinated atoms. The dihedral angles between the coordinated or uncoordinated pyridyl groups and the triazole ring are very similar to those observed in **1–3** (4.7 and 9.4° on average, respectively).

In the nca anion (**4**), electronic delocalization is observed as evidenced by the N–N (1.354(3) Å) and C–N (1.325(3) Å) bond lengths, which are shorter than typical N–N (1.47 Å) or C–N (1.43 Å) bond lengths. The geometry and bond lengths and angles in the NCSe (**5**) and ndcm (**6**) ligands are very similar to those observed in other coordination complexes involving these ligands[35] (Table S3†).

Packing in **4–6** involves face-to-face interactions (Table S5†) and strong intermolecular N–H···N and N–H···O hydrogen bonds (Table S4†). In **5**, only one intermolecular N–H···Se hydrogen bond with a hydrogen–acceptor distance of 2.76(5) Å occurs. This value is similar to those observed in other complexes containing NCSe ligands.[36]

The same interlayer π–π stacking between the coordinated and uncoordinated pyridyl rings from the neighboring complexes occurs in **4–6**; the distances between the mean planes in each pair of pyridyl rings range from 3.64 to 3.75 Å. Moreover, the same intramolecular hydrogen bond as that in **1–3**, namely $N40–H_nN···N60$ (n = 1 in **4** and 2 in **5** and **6**), between the non-coordinated pyridyl and triazole rings of abpt is observed too.

In the crystal structure of **4**, strong hydrogen bonds lead to the formation of 2D supramolecular layers in the *bc* plane (Fig. S4†), while π–π stacking interactions contribute to the higher stabilization of these layers. Similarly, in **5**, N–H···Se hydrogen bonds create layers in the $(10\bar{2})$ plane, which are further stabilized through π–π interactions which occur between the coordinated and uncoordinated pyridyl rings of abpt from neighboring molecules (Fig. S5†). On the other hand, examination of the crystal packing in **6** revealed that this compound had a similar molecular arrangement to that of the $[Co(abpt)_2(tcm)_2]$ compound[23] described earlier: one strong intermolecular N–H···N hydrogen bond creates an infinite 1D supramolecular chain running in the $[10\bar{1}]$ direction (Fig. S6†). Individual chains are connected through intermolecular π–π interactions occurring between the centroids of the adjacent coordinated and uncoordinated

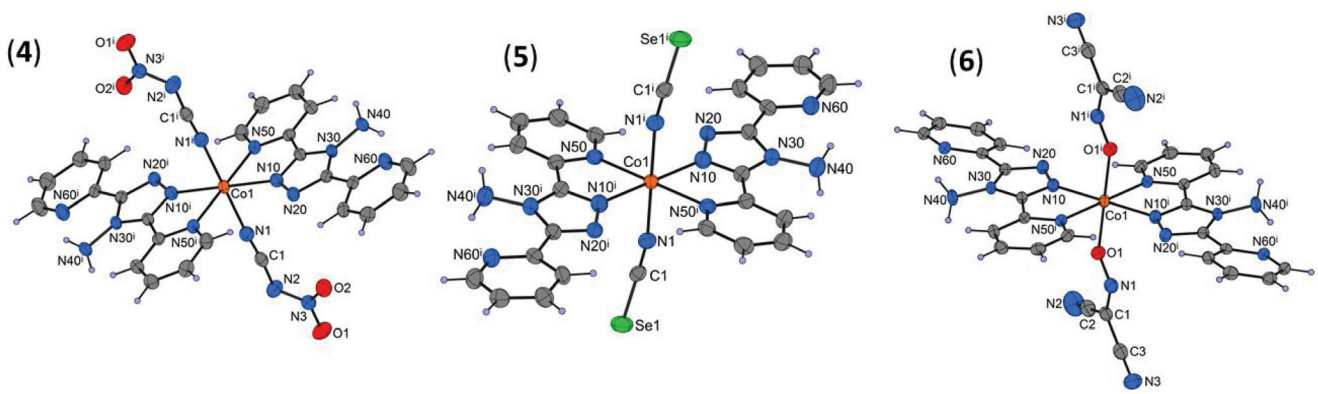

Fig. 2 Molecular structures of **4–6** with displacement ellipsoids (50% probability). [Symmetry codes: (i) 1 – *x*, 1 – *y*, –*z* (**4**), (i) –*x*, –*y*, –*z* (**5**), and 1 – *x*, –*y*, 1 – *z* (**6**)].

Open Access Article. Published on 19 December 2017. Downloaded on 9/21/2024 9:05:42 PM.
This article is licensed under a Creative Commons Attribution-NonCommercial 3.0 Unported Licence.

pyridyl rings (Fig. S6†), thus creating a 3D supramolecular network.

Magnetic properties

Static magnetic measurements and *ab initio* calculations. The temperature- and field-dependent experimental magnetic data for **1–6** are depicted in Fig. 3. The effective magnetic moments (μ_{eff}) at room temperature vary from 4.6–5.0μ_B and are higher than the spin-only value for $S = 3/2$ ($\mu_{eff}/\mu_B = 3.9$) calculated with $g = 2.0$, which indicates a non-negligible contribution of the spin–orbit coupling to the ground state and thus $g > 2.0$. A gradual drop of the effective magnetic moment down to 3.5–3.8μ_B is observed for all the compounds on lowering the temperature, which indicates significant magnetic anisotropy typically expressed within the zero-field splitting formalism. This is correspondingly demonstrated in the isothermal magnetization data where $M_{mol}/N_A\mu_B$ at $T = 2$ K and $B = 5$ or 9 T reached values of 2.1–2.3, which are much lower than the theoretical limit value of $M_{mol}/N_A\mu_B \rightarrow g{\cdot}S$. Before studying the magnetism of the hexacoordinate compounds reported here, it must be stated that in the case of octahedral Co(II) complexes, the ^4F atomic term is split into the $^4T_{1g}$ ground state and excited $^4T_{2g}$ and $^4A_{2g}$ states, and as the ground state possesses unquenched orbital angular momentum, the spin Hamiltonian formalism is not applicable.[37] Upon lowering the symmetry of the coordination polyhedron, *e.g.* from O_h to D_{4h} symmetry, the $^4T_{1g}$ ground state is further split, but it does not automatically enable utilization of the spin Hamiltonian because only in the case of the compressed tetragonal bipyramid does the $^4A_{2g}$ ground term validate such an approach,

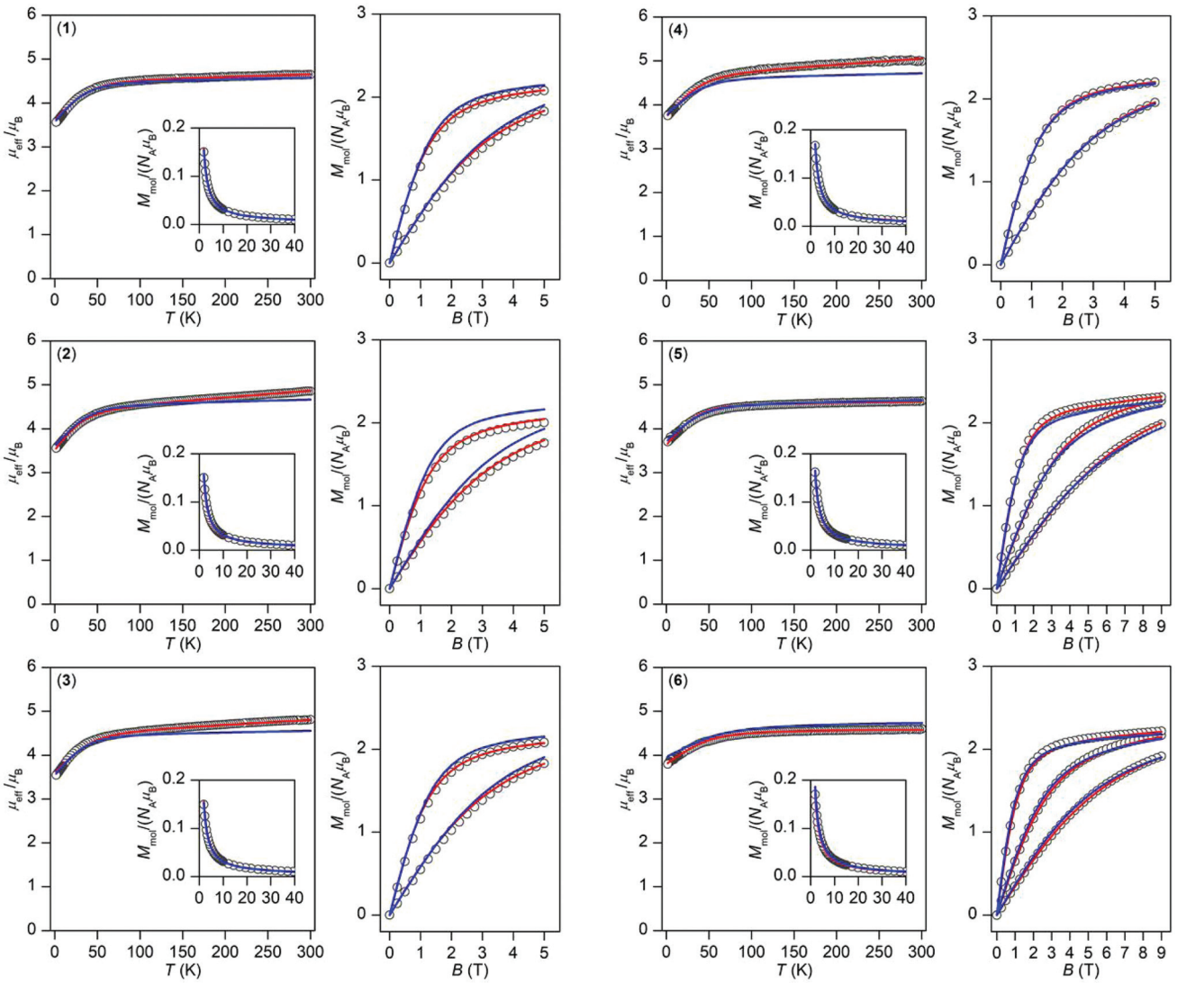

Fig. 3 Magnetic data for **1–6** shown as the temperature dependence of the effective magnetic moment and molar magnetization measured at B = 0.1 T and as the isothermal magnetization measured at T = 2, 5, and 10 K. The empty circles represent the experimental data and red solid lines represent the fitted data using eqn (1) or (2) with the parameters listed in Table 1. The blue solid lines represent the calculated data using the CASSCF/NEVPT2 energy levels from CAS(7,10) calculations.

 This journal is © The Royal Society of Chemistry 2018

Open Access Article. Published on 19 December 2017. Downloaded on 9/21/2024 9:05:42 PM.
This article is licensed under a Creative Commons Attribution-NonCommercial 3.0 Unported Licence.

whereas in the case of the elongated tetragonal bipyramid, ^4E_g is the ground term and a model beyond the spin Hamiltonian must be utilized.[38] All cobalt(II) complexes **1–6** possess C_i symmetry, but the symmetry of the coordination polyhedron can be approximated with the C_{2h} symmetry point group. None of these symmetry groups have E or T irreducible representations, thus we could expect that the spin Hamiltonian is applicable for all compounds **1–6**.

However, the accidental degeneracy of low-lying states cannot be excluded due to variation of the ligand field of the axial co-ligands. Thus, two approaches can be used to describe magnetic properties. The first one is based on the spin Hamiltonian with the zero-field splitting terms defined as:

$$\hat{H} = D(\hat{S}_z^2 - \hat{S}^2/3) + E(\hat{S}_x^2 - \hat{S}_y^2) + \mu_B B g \hat{S}_a \quad (1)$$

where D and E are the single-ion axial and rhombic ZFS parameters, respectively, and the last component is the Zeeman term defined in the direction of a magnetic field as B_a = $B(\sin(\theta)\cos(\varphi), \sin(\theta)\sin(\varphi), \cos(\theta))$ with the help of polar coordinates.[39]

The second approach suitable for pseudo-octahedral complexes is based on Griffith's,[40] Lines',[41] and Figgis'[42] works, where the orbital angular momentum and spin–orbit coupling is included in the Hamiltonian:

$$\begin{aligned}\hat{H} = &-\alpha \cdot \lambda(\vec{S} \cdot \vec{L}) + \Delta_{ax}(\hat{L}_z^2 - \hat{L}^2/3) \\ &+ \Delta_{rh}(\hat{L}_x^2 - \hat{L}_y^2) + \mu_B \vec{B}(g_e \vec{S} - \alpha \vec{L})\end{aligned} \quad (2)$$

where Δ_{ax} and Δ_{rh} describe the splitting of the $^4T_{1g}$ ground term induced by lowering the symmetry, α is the orbital reduction factor, λ is the spin–orbit coupling, and g_e = 2.0023. This L–S Hamiltonian exploits the T_1–P isomorphism, thus the angular orbital momentum L is equal to 1 with the effective Lande g-factor, $g_L = -\alpha$, and this is applied to $|S, L, M_S, M_L\rangle$ functions with M_L = 0, ±1 and M_S = ±1/2, ±3/2.[43] The orbital reduction factor expresses two parameters, $\alpha = A\kappa$, where A is the Figgis coefficient of the configuration interaction resulting from the admixture of the excited terms reflecting the ligand field strength ($1 < A < 3/2$), and κ describes the lowering orbital contribution due to covalency of the metal–ligand bond and it usually holds $\kappa \leq 1$. Additionally, the spin–orbit coupling parameter λ can also be reduced in comparison with its free-ion value $\lambda_0 = -180$ cm^{-1} due to the covalent character of the donor–acceptor bond. Therefore, prior to analyzing the experimental magnetic data either using the model defined in eqn (1) or in eqn (2), *ab initio* calculations on the experimental complex geometries were performed to elucidate the electronic structure of the studied complexes and gain better insight into the low-lying multiplet energy levels. Our method of choice was the well-established post-Hartree–Fock multi-reference method based on the State-Averaged Complete Active Space Self-Consistent Field (SA-CASSCF), which was utilized to calculate all ninety energy levels resulting from the $3d^7$ electronic configuration with the ORCA computational package.[44] Actually, the active space was defined as seven electrons in five d-orbitals, CAS(7,5), and the dynamic electronic correlation was treated with the NEVPT2 method. Furthermore, the active space was enlarged to 10 orbitals (3d + 4d) to account for the double-shell effect,[45] which is supposed to be important for late 3d-metals. The calculated ligand field terms and multiplets for **1–6** are depicted in Fig. 4.

The first excited quartet term is in the range of 1123–1729 cm^{-1} for **1–5**, but in the case of **6** the energy gap is only 609 cm^{-1}. Thus it is obvious that the lowest quartet term is well separated from the excited ones only for **1–5**. This is also reflected in the ligand field multiplets calculated after including the spin–orbit coupling, where in the case of **1–5**, two lowest Kramers doublets can be described with the ZFS formalism using S = 3/2 (eqn (1)), because the third doublet is well separated from the ground state by an energy difference of 1194–1628 cm^{-1}. However, in the case of **6**, the third doublet has an energy of 780 cm^{-1}, therefore the spin Hamiltonian formalism with S = 3/2 is not applicable and the magnetic properties should be analyzed with the L–S Hamiltonian (eqn (2)). The application of the effective Hamiltonian theory for S = 3/2 resulted in the ZFS and g-tensor parameters listed in Table 2. Interestingly, the double-shell effect (CAS(7,5) *vs.* CAS(7,10)) has only a minor impact on the derived values, which can be deduced by comparing D, E, and the respective g-parameters in Table 2 (*e.g.* D = 40.0 cm^{-1} and E/D = 0.303 calculated with CAS(7,5) *vs.* D = 40.1 cm^{-1} and E/D = 0.281 calculated with CAS (7,10) for **4**). Overall, D is positive and found in a narrow range from 37.0 to 40.1 cm^{-1} with rhombicity, E/D, spanning the interval 0.065–0.290 for **1–5** and CAS(7,10). Similar analysis applied to **6** resulted in a negative D parameter and one of the g-factors being less than g_e, which indirectly confirms that the spin Hamiltonian is not applicable in this case and that these parameters have no physical meaning. Therefore, the CAS

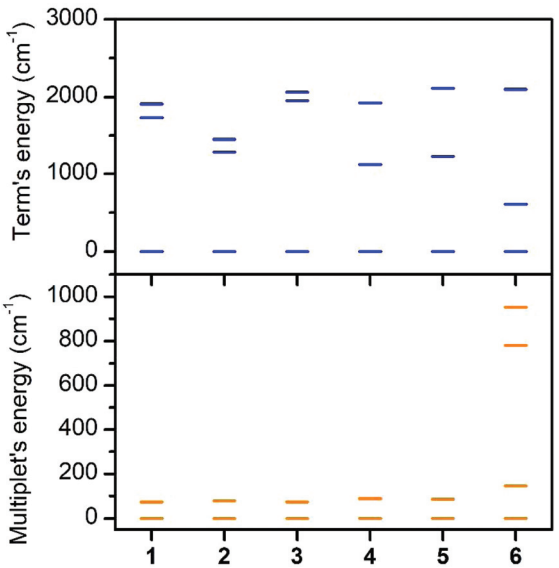

Fig. 4 The lowest energy levels from CASSCF/NEVPT2 calculations with CAS(7,10) active space for **1–6** (the quartet ligand field terms originate from the $^4T_{1g}$ atomic term (top) and the lowest ligand field multiplets/Kramers doublets result from the spin–orbit coupling (bottom)).

Open Access Article. Published on 19 December 2017. Downloaded on 9/21/2024 9:05:42 PM. This article is licensed under a Creative Commons Attribution-NonCommercial 3.0 Unported Licence.

Table 2 Comparison of CASSCF/NEVPT2 and the fitted parameters for **1–6** accompanied by AOM parameters derived from AILFT analysis

	1	2	3	4	5	6[a]
ZFS and *g* values based on CASSCF/NEVPT2 calculations with CAS(7,5)						
D (cm^{-1})	36.6	39.8	36.8	40.0	38.2	*−69.7*
E/D	0.123	0.089	0.113	0.303	0.312	*0.258*
$g_x/g_y/g_z$	2.330/2.464/2.058	2.391/2.513/2.083	2.316/2.436/2.047	2.323/2.546/2.058	2.313/2.534/2.057	*2.230/1.990/2.805*
ZFS and *g* values based on CASSCF/NEVPT2 calculations with CAS(7,10)[b]						
D (cm^{-1})	37.0	39.9	36.8	40.1	38.6	*−66.3*
E/D	0.121	0.065	0.095	0.281	0.290	*0.270*
$g_x/g_y/g_z$	2.340/2.475/2.055	2.410/2.508/2.082	2.329/2.435/2.044	2.335/2.551/2.058	2.326/2.542/2.056	*2.240/1.991/2.797*
$U_{calc.}$ (cm^{-1})	75.6	80.2	74.6	89.1	86.5	146.5
f	0.986	0.971	0.999	1.010	0.991	0.950
Analysis of the experimental magnetic data						
D (cm^{-1})	34.9	31.0	37.8	41.4	37.7	$\Delta_{ax} = -1345$ cm^{-1}
E/D	0.327	0.333	0.308	0.228	0.135	$\Delta_{rh}/\Delta_{ax} = 0.174$ cm^{-1}
g_{xy}/g_z	2.42/2.00	2.36/2.00	2.41/2.00	2.53/2.00	2.46/2.00	$\lambda = -180$ cm^{-1}
χ_{TIP}	9.1	23.9	17	22	5.0	$\alpha = 1.23$
$U_{calc.}$ (cm^{-1})	80.3	71.6	85.7	89.0	77.4	108
AILFT and AOM analysis of CASSCF/NEVP2 calculations with CAS(7,5)						
B (cm^{-1})	1056	1055	1062	1050	1051	1052
C (cm^{-1})	3992	3997	3956	3973	3966	3985
ξ (cm^{-1})	524	524	524	524	524	524
$e_\sigma^{tr}/e_{\pi s}^{tr}$	4274/−244	3919/−499	4658/34	4000/−76	4042/73	3705/−183
$e_\sigma^{py}/e_{\pi s}^{py}$	3491/−856	3891/−399	3728/−711	3770/−103	3461/−67	3864/74
e_σ^{ax}/e_π^{ax}	2375/992	2394/935	2693/1064	3662/1020	3807/991	3517/1174

[a] The first excited state is relatively close to the ground spin state. [b] f is a scaling factor used to obtain the best match with the experimental magnetic data.

(7,10)-CASSCF/NEVPT2 energies of the lowest six Kramers doublets originating from the $^4T_{1g}$ term of **6** were analyzed with the Hamiltonian in eqn (2) and we found these parameters to be: $\alpha\cdot\lambda$ = −223 cm^{-1}, Δ_{ax} = −1803 cm^{-1}, and Δ_{rh} = −319 cm^{-1} (Δ_{rh}/Δ_{ax} = 0.176) (Fig. S7†). To validate the *ab initio* calculations, we employed the calculated CAS(7,10)-CASSCF/NEVPT2 matrices of the spin–orbit coupling (H^{SOC}), the spin momentum (S_x, S_y, S_z), and the orbital momentum (L_x, L_y, L_z) operators to calculate the energy levels for any strength and orientation of the magnetic field by diagonalization of the matrix **H** defined as:

$$\mathbf{H} = \mathbf{H}^{SOC} + \mu_B(\mathbf{L} + g_e\mathbf{S}) \quad (3)$$

This enabled us to calculate the partition function and the integral average of the molar magnetization.[23] The great benefit of this procedure is the fact that no restriction of the spin Hamiltonian formalism is applied, thus no ZFS or *g*-tensor parameters are used. The calculated data are compared to the experimental magnetic data in Fig. 3 and we can conclude that there is good agreement with the low temperature data for all of the compounds; only in the case of **2** is a somewhat larger deviation in the isothermal magnetization found. This shows that a multi-configuration method such as CASSCF/NEVPT2 used here is well-suited for treating the magnetism of Co(II) complexes.

Thus, the outcomes of these calculations were used in fitting the experimental magnetic data of **1–6**. Therefore, the spin Hamiltonian model in eqn (1) was used for compounds **1–5**, while the *L–S* Hamiltonian was applied for compound **6**. In all cases, the molar magnetization (M_{mol}) was calculated from the partition function (Z) for a given direction of a magnetic field $B_a = B\cdot(\sin\theta\cos\varphi, \sin\theta\sin\varphi, \cos\theta)$ as:

$$M_{mol} = N_A \frac{d\ln Z}{dB_a} \quad (4)$$

Then, the integral (orientational) average of molar magnetization was calculated

$$M_{mol} = 1/4\pi \int_0^{2\pi}\int_0^{\pi} M_a \sin\theta d\theta d\varphi \quad (5)$$

to properly simulate the experimental powder magnetization data. Furthermore, both temperature- and field-dependent magnetic data were fitted simultaneously to achieve trustworthy parameters. The resulting parameters are listed in Table 2 and fitted data are visualized in Fig. 3. In most cases, there is good agreement between the fitted parameters and the ones calculated by CASSSCF/NEVPT2, *e.g.* in the case of **4**, the fitted D is 41.4 cm^{-1} while the calculated D is 40.1 cm^{-1}. The largest discrepancies are found for **2**, where the fitted D is 31.0 cm^{-1} and the calculated value is 39.9 cm^{-1}.

To gain better insight into the relationship between the coordination polyhedron geometry and the magnetic properties, the Mayer bond orders with the CAM-B3LYP DFT functional were also calculated and are plotted in Fig. 5 together with the donor–acceptor bond distances and octahedral distortion parameter Σ. It is evident that the bond orders among the

 This journal is © The Royal Society of Chemistry 2018

Open Access Article. Published on 19 December 2017. Downloaded on 9/21/2024 9:05:42 PM.
This article is licensed under a Creative Commons Attribution-NonCommercial 3.0 Unported Licence.

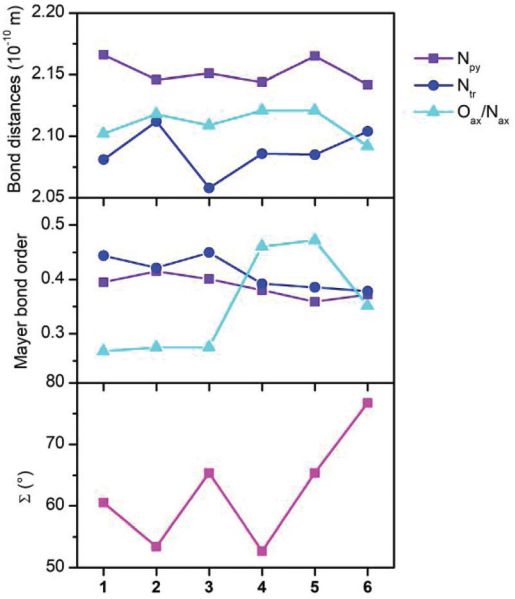

Fig. 5 Bond distances, Mayer bond orders from CAM-B3LYP calculations, and the octahedron distortion parameter Σ.

cobalt and nitrogen atoms of the abpt ligand are only slightly varied within **1–6**. In the case of the axial ligands, the bond order increases as $Co–O_{H_2O} \approx Co–O_{MeOH} < Co–O_{ndcm} < Co–N_{nca} < Co–N_{NCSe}$.

Moreover, we also used another approach based on the Angular Overlap Model (AOM) to better understand the electronic structure of the reported complexes.[46] This ligand field theory classifies ligands as σ-donors, σ-donors and π-donors, and σ-donors and π-acceptors utilizing molecular orbitals between a metal atom and donor atoms. The AOM quantifies the effect of the ligands on the d-orbital splitting with e_σ, $e_{\pi s}$, and $e_{\pi c}$ parameters. Here, e_σ measures the σ-type molecular overlap and logically always has a positive value due to the formation of donor–acceptor bonds, whereas the π-type molecular overlap can be anisotropic ($e_{\pi s} \neq e_{\pi c}$) and can adopt positive or negative values for π-donors or π-acceptors. Recently, the *ab initio* ligand field theory (AILFT) was developed based on CASSCF (CASSCF/NEVPT2) calculations for d-metal coordination compounds and was implemented in ORCA software.[47] The AILFT analyses of **1–6** based on CASSCF/NEVPT2 calculations with CAS(7,5) resulted in the Racah parameters (B and C) and ligand field matrix (V^{LFT}) describing the effective ligand field potential acting on the metal d-orbitals. In the next step, we analyzed this V^{LFT} matrix with the AOM using the AOMX program,[48] which enabled us to derive the AOM parameters for **1–6**. In these calculations, six parameters were varied in total, namely the σ-parameters of the triazole N-donor atoms (e_σ^{tr}) and pyridine N-donor atoms (e_σ^{py}) stemming from the abpt ligand, and e_σ^{ax} of the axial O/N donor atoms of the solvent or coordinated pseudohalide ligands. The π-type interactions of the axial donor atoms were considered as isotropic ($e_{\pi s}^{ax} = e_{\pi c}^{ax} = e_\pi^{ax}$), whereas the π-type interactions of the planar donor atoms of abpt were considered as anisotropic: the in-plane π-interactions were assumed to be negligible ($e_{\pi c}^{tr} = e_{\pi c}^{py} = 0$) and the π-type interactions perpendicular to the abpt plane were varied freely ($e_{\pi s}^{tr} \neq e_{\pi s}^{py} \neq 0$). The results of this analysis are depicted in Fig. 6 and listed in Table 2. The σ-type AOM parameters of **1–6** nicely copy the trend observed from the DFT calculations of the Mayer bond order (Fig. 5). The axial donor atoms O_{ndcm}, N_{NCSe}, and N_{nca} are stronger σ-donors than O_{H_2O} and O_{MeOH}, whereas their π-donor properties are about the same; the maximal value was found for O_{ndcm} in **6**. The abpt ligand acts as a strong σ-donor with π-acceptor properties in **1–3**, whereas the $e_{\pi s}^{tr}$ and $e_{\pi s}^{py}$ parameters are close to zero in **4–6**. The calculated AOM parameters revealed that the equatorial abpt ligands impose a stronger ligand field than the axially coordinated molecules of the solvents or pseudohalide ligands, which means that this situation resembles the case of the elongated tetragonal bipyramid with the ^4E_g ground term. This would imply that the *L–S* model (eqn (2)) is appropriate for this series, but CASSCF/NEVPT2 calculations showed that this model is suitable only for compound **6**. To better understand this phenomenon, the AOM was used, in which two factors were studied: (i) the size of the bite angle of the equatorial bidentate ligand and (ii) the ligand field strength of the axial ligand. The AOMX program was employed using the average values of the AOM parameters found for **1–6** as B = 1054 cm^{-1}, C = 3978 cm^{-1}, and ξ = 524 cm^{-1}, and the equatorial ligands were simulated with e_σ^{eq} = 3900 cm^{-1} and $e_{\pi s}^{eq}$ = −250 cm^{-1} with a varying bite angle α = 60–90°. The AOM parameters of the axial ligands were e_σ^{ax} = 2000–4000 cm^{-1} with e_π^{ax} = 1000 cm^{-1}. The energy gap between the two lowest Kramers doublets (Δ_{1-2}) and the energy of the third Kramers doublet (Δ_{1-3}) are visualized in a 2D contour plot in Fig. 7. Evidently, the bite angle α has a dramatic effect on the multi-

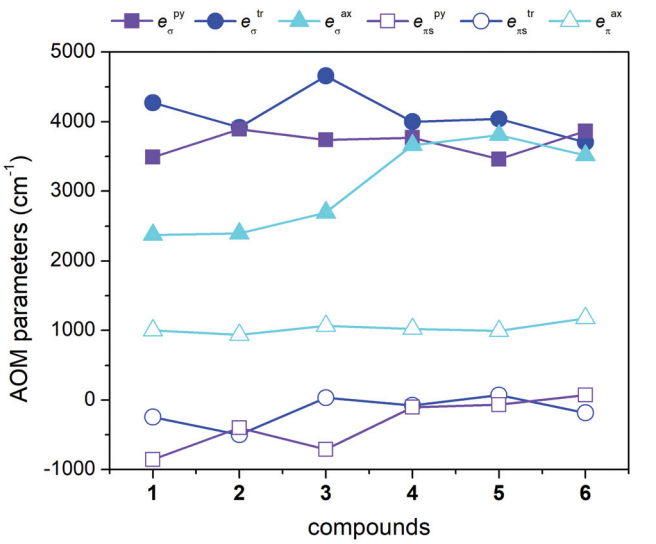

Fig. 6 AOM analysis using the AILFT applied on CASSCF/NEVPT2 calculations with CAS(7,5) for **1–6**. The σ-type and π-type AOM parameters are plotted as filled and empty points, respectively.

Open Access Article. Published on 19 December 2017. Downloaded on 9/21/2024 9:05:42 PM.
This article is licensed under a Creative Commons Attribution-NonCommercial 3.0 Unported Licence.

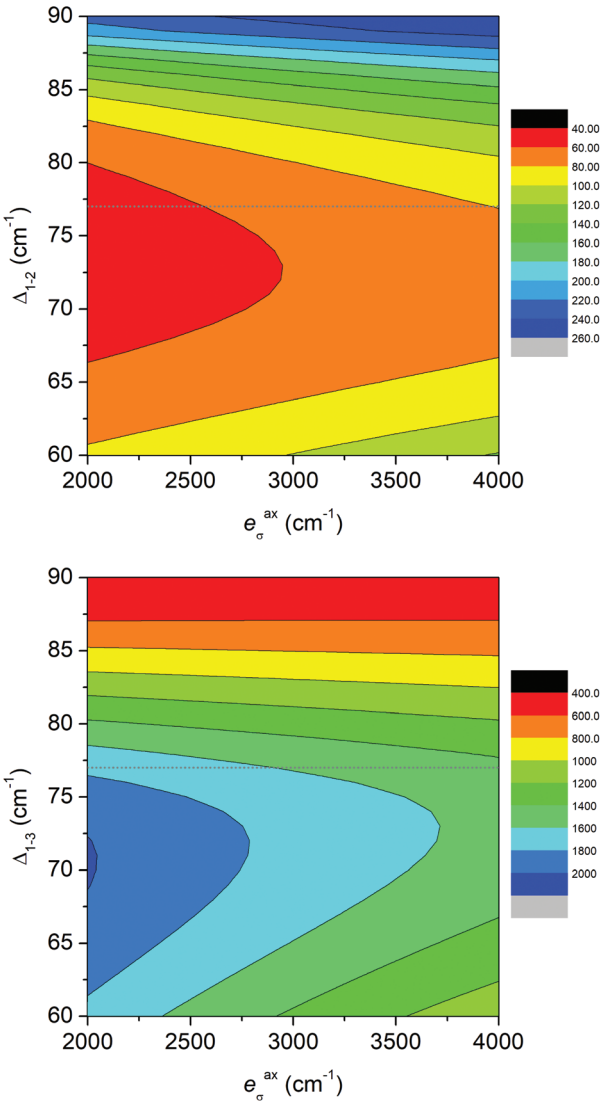

Fig. 7 The AOM for hexacoordinate complexes **1–6** using B = 1054 cm^{-1}, C = 3978 cm^{-1}, and ξ = 524 cm^{-1}, where the equatorial bidentate ligands were simulated with e_σ^{eq} = 3900 cm^{-1} and $e_{\pi s}^{eq}$ = −250 cm^{-1} with a varying bite angle α = 60–90°, and the axial ligands were simulated with e_σ^{ax} = 2000–4000 cm^{-1} and e_π^{ax} = 1000 cm^{-1}. Δ_{1-2} and Δ_{1-3} are the energies of the second and third Kramers doublets, respectively. The dotted gray line shows α = 77°, a typical value for the abpt ligand.

plet levels; a decrease in α led to a decrease in Δ_{1-2}, but on the other hand, to an increase in Δ_{1-3}. Next, the increase in e_σ^{ax} resulted in an increase in Δ_{1-2} and a decrease in Δ_{1-3} for smaller values of the bite angle. Taking into account the average bite angle for the abpt ligand ($\alpha \approx$ 76–77°, Tables S2 and S3†), these findings explain why the spin Hamiltonian formalism is applicable for most of the reported compounds (Δ_{1-3} is larger than 1000 cm^{-1}). Also, this modelling explains why despite the large variation of the axial ligands and their ligand field strength, the ZFS energy gap only varies a little for **1–6**. To summarize, this magneto–structural correlation based on AOM theory helped us to better understand the impact of the abpt and various axial co-ligands on the magnetic levels in the reported compounds.

Dynamic magnetic measurements

The AC susceptibility was measured to study the dynamic magnetic properties of **1–6**. We did not find out-of-phase signals in a zero static magnetic field, but upon turning on the magnetic field, the imaginary susceptibility became non-zero for all compounds (Fig. S8–S13†). Then, the AC susceptibility was measured at B_{DC} = 0.1 T and revealed frequency-dependent maxima of the imaginary susceptibility for **1–2** and **4–6**, whereas in the case of **3**, the signal is frequency-dependent but without maxima (Fig. S14†). This confirms the slow relaxation of the magnetization in **1–6** as a typical feature of SMMs. Moreover, in all the compounds we observed only one relaxation process, which indirectly indicates that cobalt complexes are well-separated in the solid state and there are no efficient exchange pathways to induce other relaxation processes as was reported for other Co(II) SIMs.[49] Thus, the experimental data were then analyzed with the one-component Debye's model based on eqn (6):

$$\chi(\omega) = \frac{\chi_T - \chi_S}{1 + (i\omega\tau)^{1-\alpha}} + \chi_S \quad (6)$$

which resulted in isothermal (χ_T) and adiabatic (χ_S) susceptibilities, relaxation times (τ), and distribution parameters (α) (Tables S6–S10†). This enabled us to construct the Argand (Cole–Cole) plot (Fig. 8 and 9 and Fig. S15–S17†). Subsequently, a linear fit to the Arrhenius law was applied for the highest temperatures, which revealed values of τ_0 and U_{eff} parameters for **1–2** and **4–6** as listed in Table 3. The effective spin reversal barrier U_{eff} varies between 12 and 44 K.

As well as the Arrhenius law, we also tried to fit all relaxation times to the combination of the direct (A) and Orbach (τ_0 and U) relaxation processes as:

$$\frac{1}{\tau} = AT + \frac{1}{\tau_0}\exp(-U/kT) \quad (7)$$

and the results are shown in Fig. 8 and 9 and Fig. S15–S17† with the parameters listed in Table 3. The derived U_{eff} values are similar to those found by the Arrhenius law and lie in the range of 12–27 K. An alternative relaxation mechanism is the Raman process, therefore the relaxation times were also fitted with following equation:

$$\frac{1}{\tau} = AT + CT^n \quad (8)$$

comprising the one-phonon direct (A) and two-phonon Raman (C and n) processes. The values of the A parameter are close to those found by eqn (7) (Table 3). The Raman coefficient n was found between 2.55 and 6.64. Generally, n = 9 is expected for well-separated Kramers doublets,[50] however usually n < 9 is reported for Co(II) complexes.

Both of these approaches (eqn (7) and (8)) can elucidate the temperature dependence of the relaxation time for **1–2** and **4–6**, but are limited only to the AC data having maxima in the

 This journal is © The Royal Society of Chemistry 2018

Open Access Article. Published on 19 December 2017. Downloaded on 9/21/2024 9:05:42 PM.
This article is licensed under a Creative Commons Attribution-NonCommercial 3.0 Unported Licence.

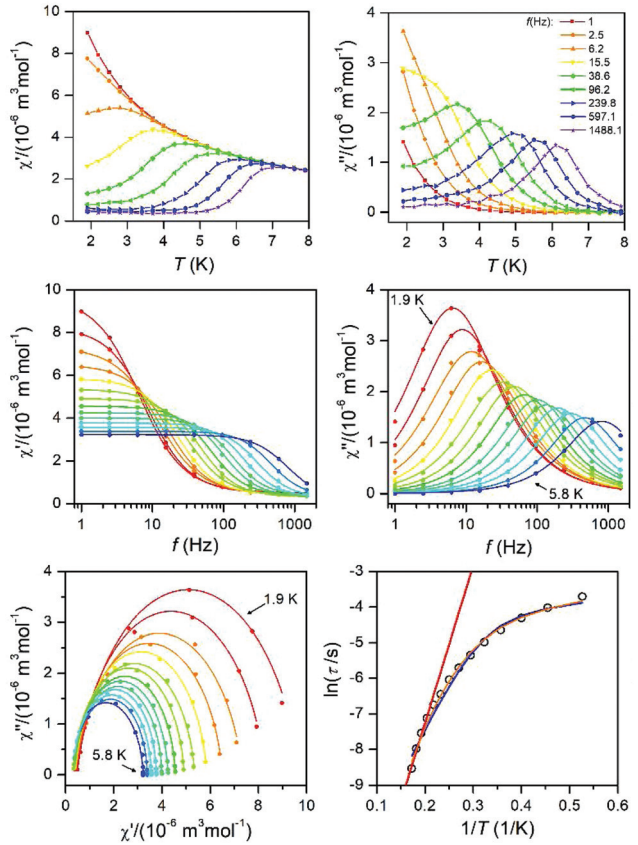

Fig. 8 AC susceptibility data for **1**. Top: In-phase χ' and out-of-phase χ'' molar susceptibilities at the applied external magnetic field B_{DC} = 0.1 T (solid lines are only guides for the eyes). Middle: Frequency dependence of the in-phase χ' and out-of-phase χ'' molar susceptibilities fitted with the one-component Debye's model using eqn (6) (solid lines). Bottom: the Argand (Cole–Cole) plot with solid lines fitted with eqn (6), with on the left side the fit of the resulting relaxation times τ with the Arrhenius law (red line), and the combination of the direct and Orbach processes (blue line) using eqn (7) and the combination of the direct and Raman processes (orange line) using eqn (8).

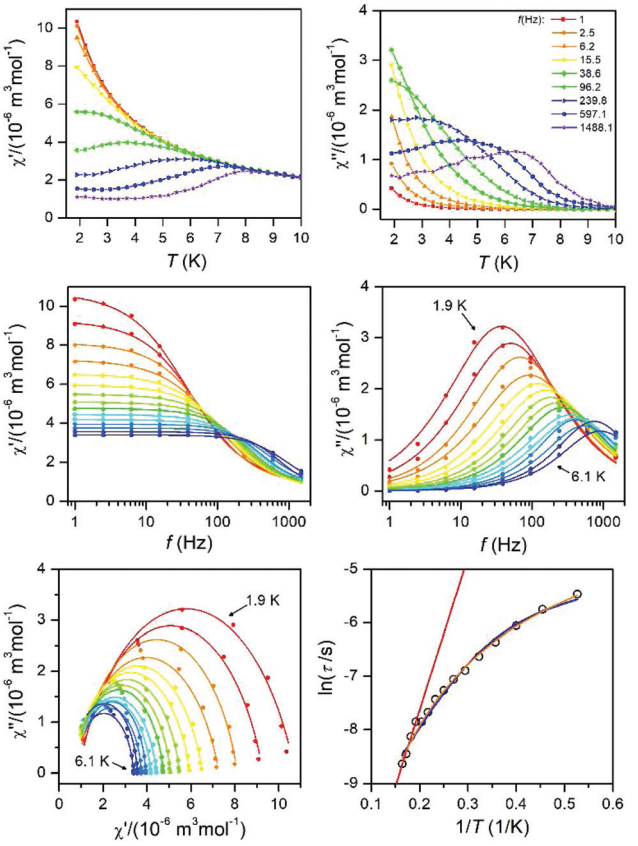

Fig. 9 AC susceptibility data for **6**. Top: In-phase χ' and out-of-phase χ'' molar susceptibilities at the applied external magnetic field B_{DC} = 0.1 T (solid lines are only guides for the eyes). Middle: Frequency dependence of the in-phase χ' and out-of-phase χ'' molar susceptibilities fitted with the one-component Debye's model using eqn (6) (solid lines). Bottom: The Argand (Cole–Cole) plot with solid lines fitted with eqn (6), with on the left side the fit of the resulting relaxation times τ with the Arrhenius law (red line), and the combination of the direct and Orbach processes (blue line) using eqn (7) and the combination of the direct and Raman processes (orange line) using eqn (8).

Argand diagram, while non-zero out-of-phase AC susceptibility was observed at higher temperatures, which means that such an analysis of thermally activated mechanisms can be biased. Therefore, the AC susceptibility data were also analyzed with a simplified model, which is derived under the assumption that the adiabatic susceptibility is usually approaching zero in single-molecule magnets ($\chi_S \rightarrow 0$) for highest temperatures.[3a] Then the following equation

$$\ln(\chi''/\chi') = \ln(2\pi f \tau_0) + U_{eff}/kT \quad (9)$$

holds for the Orbach relaxation process or alternatively the equation

$$\ln(\chi''/\chi') = \ln(2\pi fC) - n\ln T \quad (10)$$

holds for the Raman relaxation process. The AC data for the two highest frequencies were employed for both equations (Fig. S18 and S19†) and the calculated parameters are listed in Table 3. U_{eff} was found in the range from 17 to 104 K for **1–6.** These values, except for those for **3**, are rather close to the expected $U_{calc.}$ values listed in Table 2. In contrast, the application of eqn (10) resulted in a Raman coefficient n greater than 9 for **1–2** and **4–5**, which lacks physical meaning. Thus, in our opinion, in the high temperature region, both the Orbach and Raman relaxation processes could be present to a varying extent across the series, whereas the direct relaxation process dominates in the low temperature region.

Experimental

Materials and methods

$N\{C(CN)_2\}_2$ (1,1,3,3-tetracyano-2-azapropenide, tcap), $NO_2C(CN)_2$ (nitrodicyanomethanide, nodcm), $C(CN)\{C(CN)_2\}_2$ (1,1,2,3,3-pentacyanopropenide, pcp), NO_2NCN (nitrocyanamide, nca), and $ONC(CN)_2$ (nitrosodicyanomethanide, ndcm) in the form of potassium or sodium salts were synthesized at

Open Access Article. Published on 19 December 2017. Downloaded on 9/21/2024 9:05:42 PM.
This article is licensed under a Creative Commons Attribution-NonCommercial 3.0 Unported Licence.

Table 3 Summary of the Orbach relaxation mechanism parameters for **1–6**

	Arrhenius law		Direct and Orbach (eqn (7))			Direct and Raman (eqn (8))			Orbach simplified model (eqn (9))		Raman simplified model (eqn (10))	
	τ_0 (s)	U_{eff} (K)	A (K^{-1} s^{-1})	τ_0 (10^{-6} s)	U_{eff} (K)	A (K^{-1} s^{-1})	C (K^{-n} s^{-1})	n	τ_0 (s)	U_{eff} (K)	C (K^{-n} s^{-1})	n
1	1.04×10^{-7}	44.1	25.2	2.60	27.4	23.1	0.0345	6.64	2.49×10^{-11}	95.6[a]	5.14×10^{6}	13.4[a]
									4.88×10^{-10}	73.8[b]	1.26×10^{4}	10.4[b]
2	2.96×10^{-5}	12.3	137	29.5	14.0	99.5	9.14	3.49	3.72×10^{-12}	104[a]	1.48×10^{8}	15.5[a]
									3.51×10^{-10}	71.8[b]	1.84×10^{4}	10.9[b]
3	—	—	—	—	—	—	—	—	2.42×10^{-7}	18.9[a]	6.19×10^{-3}	3.94[a]
									3.11×10^{-7}	17.1[b]	2.09×10^{-3}	3.35[b]
4	2.19×10^{-5}	12.0	459	25.9	15.6	413	9.75	3.30	7.78×10^{-9}	59.1[a]	1.37×10^{5}	11.2[a]
									3.74×10^{-9}	64.1[b]	3.24×10^{3}	9.40[b]
5	7.76×10^{-6}	17.0	245	25.2	12.7	82.9	65.5	2.55	3.66×10^{-9}	67.5[a]	1.44×10^{4}	9.83[a]
									1.36×10^{-9}	74.0[b]	1.83×10^{4}	10.0[b]
6	1.63×10^{-6}	28.5	131	17.1	16.4	76.1	11.4	3.32	$4.4.5 \times 10^{-9}$	68.1[a]	4.44×10^{2}	8.08[a]
									1.59×10^{-8}	57.1[b]	4.97×10^{1}	7.06[b]

[a] Calculated for f = 1488 Hz. [b] Calculated for f = 716 Hz.

the Martin Luther University in Halle, Germany. All other chemicals are commercially available and were used without further purification. Elemental analysis of C, H, and N was carried out using a CHNOS Elemental Analyzer vario MICRO (Elementar Analysensysteme GmbH). The infrared spectra of the complexes were recorded on a Nicolet 6700 FT-IR spectrophotometer (Thermo Scientific) equipped with a diamond crystal Smart Orbit™ in the range 4000–400 cm^{-1}. The temperature-dependent (T = 1.9–300 K, B = 0.1 T) and field-dependent (B = 0–5 T, T = 2 or 5 K, or B = 0–9 T, T = 2, 5, or 10 K) magnetization measurements were performed on an MPMS XL-7 SQUID magnetometer (Quantum design Inc., San Diego, CA, USA) or PPMS Dynacool (Quantum design Inc., San Diego, CA, USA). Dynamic magnetic properties were studied by measuring the alternating current (AC) susceptibility on a MPMS XL-7 SQUID magnetometer. The magnetic data were corrected for the diamagnetism of the constituent atoms and for the diamagnetism of the sample holder.

Synthesis

Complexes **1–4** were prepared by the same method. A methanol solution (5 mL) of abpt (0.15 mmol, 35.7 mg) was added to a solution of $CoCl_2$ (0.075 mmol, 17.8 mg $CoCl_2{\cdot}6H_2O$) in water (5 mL). The resulting light-yellow solution was mixed with a methanol solution (5 mL) comprising 0.15 mmol of appropriate pseudohalide (27.2 mg tcap, 22.4 mg nodcm, 21.2 mg pcp, or 18.7 mg nca). Yellow powder precipitates of **1–4** were almost immediately formed, filtered off, washed with a small amount of water, and dried in air. The final solutions were allowed to evaporate for a week, giving yellow crystals of **1–4** suitable for X-ray studies, which were filtered off and dried in air.

$[Co(abpt)_2(H_2O)_2](N\{C(CN)_2\}_2)_2{\cdot}H_2O$ (1). Yield: 48%. Anal. calc. for $C_{36}H_{22}N_{22}O_3Co$: C, 49.49; H, 3.00; N, 35.27. Found: C, 49.18; H, 3.08; N, 34.53. IR data (cm^{-1}): 3414(br), 3230(br), 3189(br), 3102(br), 2221(w), 2202(s), 2191(s), 1653(m), 1606(m), 1593(m), 1572(m), 1462(s), 1431(s), 1402(m), 1315(m), 1294(m), 1286(m), 1255(m), 1234(m), 1078(m), 1051(m), 1040(m), 1013(m), 988(m), 797(s), 787(s), 750(s), 744(s), 697(s), 606(m), 525(w), 504(w), 477(m), 420(m).

$[Co(abpt)_2(H_2O)_2](NO_2C(CN)_2)_2$ (2). Yield: 52%. Anal. calc. for $C_{30}H_{24}N_{18}O_6Co$: C, 44.51; H, 3.24; N, 31.14. Found: C, 44.53; H, 2.88; N, 30.70. IR data (cm^{-1}): 3390(br), 3319(br), 3250(br), 3189(br), 3110(w), 3101(w), 3064(w), 3049(w), 2220(s), 2202(s), 1646(m), 1605(m), 1588(m), 1570(m), 1462(s), 1491(s), 1414(s), 1337(s), 1295(m), 1273(m), 1244(s), 1164(m), 1153(m), 1051(m), 1030(s), 1015(m), 983(m), 804(m), 796(s), 758(s), 746(s), 700(s), 635(m), 607(m), 528(m), 490(w), 449(w), 418(m).

$[Co(abpt)_2(CH_3OH)_2](C(CN)\{C(CN)_2\}_2)_2$ (3). Yield: 46%. Anal. calc. for $C_{42}H_{28}N_{22}O_2Co$: C, 54.14; H, 3.03; N, 33.07. Found: C, 53.86; H, 2.80; N, 32.67. IR data (cm^{-1}): 3469(br), 3383(br), 3257(br), 3189(br), 3070(w), 3018(w), 2227(w), 2200(s), 1637(m), 1606(m), 1593(m), 1572(m), 1501(s), 1491(s), 1456(m), 1431(m), 1297(m), 1290(m), 1255(m), 1156(m), 1051(m), 1037(m), 1012(m), 987(m), 789(s), 752(s), 741(s), 701(s), 666(m), 607(m), 534(s), 489(w), 451(w), 420(m).

$[Co(abpt)_2(NO_2NCN)_2]$ (4). Yield: 44%. Anal. calc. for $C_{26}H_{20}N_{18}O_4Co$: C, 44.14; H, 2.85; N, 35.64. Found: C, 44.34; H, 2.80; N, 35.09. IR data (cm^{-1}): 3236(br), 3193(br), 3165(w), 3070(w), 3059(w), 3020(w), 2204(s), 1641(w), 1606(m), 1589(m), 1572(m), 1491(m), 1472(s), 1463(s), 1447(m), 1425(m), 1302(m), 1291(m), 1253(m), 1173(m), 1146(m), 1112(m), 1089(m), 1062(m), 1016(m), 997(m), 988(m), 941(m), 790(s), 768(m), 748(s), 743(s), 711(m), 698(s), 642(m), 634(m), 607(m), 546(s), 500(w), 491(w), 453(w), 420(m).

Single crystals of **5** and **6** were obtained at the interfaces of layered systems in large test tubes, with the lower layers comprising an aqueous solution (6 mL) of cobalt(II) nitrate (0.2 mmol, 58.21 mg $Co(NO_3)_2{\cdot}6H_2O$) (**5**) or chloride (47.6 mg $CoCl_2{\cdot}6H_2O$) (**6**) and NCSe (0.2 mmol, 21.0 mg KNCSe) (**5**) or ndcm (0.2 mmol, 23.41 mg $NaONC(CN)_2$) (**6**) and the upper layers comprising an ethanolic solution (5 mL) of abpt (0.2 mmol, 47.65 mg). These layered systems were allowed to stand undisturbed at room temperature. Yellow crystals of **5**

 This journal is © The Royal Society of Chemistry 2018

Open Access Article. Published on 19 December 2017. Downloaded on 9/21/2024 9:05:42 PM.
This article is licensed under a Creative Commons Attribution-NonCommercial 3.0 Unported Licence.

and **6** suitable for X-ray analysis were obtained and filtered off after 2 weeks and dried in air.

$[Co(abpt)_2(NCSe)_2]$ (5). Yield: 39%. Anal. calc. for $C_{26}H_{20}N_{14}Se_2Co$: C, 41.90; H, 2.70; N, 26.31. Found: C, 41.59; H, 2.49; N, 25.86. IR data (cm^{-1}): 3183(br, w), 3120(w), 3001(w), 2920(w), 2850(w), 2083(s), 1601(m), 1589(m), 1570(m), 1487(m), 1460(m), 1451(s), 1424(m), 1298(m), 1283(m), 1255(m), 1166(m), 1148(m), 1109(m), 1088(m), 1059(m), 1050(m), 1012(m), 987(m), 899(m), 786(s), 744(s), 743(s), 695(s), 635(m), 606(m), 488(w), 454(w), 419(m).

$[Co(abpt)_2(ONC(CN)_2)_2]$ (6). Yield: 47%. Anal. calc. for $C_{30}N_{18}H_{20}O_2Co$: C, 49.80; H, 2.79; N, 34.85. Found: C, 49.54; H, 2.80; N, 34.69. IR data (cm^{-1}): 3280 (m), 3192(w), 3078(w), 3022(w), 2218(m), 2212(m), 1635(m), 1605(m), 1590(m), 1568(m), 1489(m), 1456(m), 1428(m), 1340(m), 1301(m), 1257(m), 1220(s), 1151(m), 1093(m), 1056(m), 1031(m), 984(w), 802(m), 793(s), 747(s), 711(m), 700(s), 642(m), 633(m), 592(w), 578(w), 492(m), 420(m).

Crystallography

Diffraction data for **1–6** were collected at 173 K using an Oxford Diffraction Xcalibur2 diffractometer equipped with a Sapphire2 CCD detector using graphite monochromated MoKα radiation (λ = 0.71073 Å). Crysalis CCD was used for data collection while Crysalis RED was used for cell refinement, data reduction, and absorption correction.[51] The structures were solved by SUPERFLIP[52] and refined against the F^2 data using full matrix least squares methods with the program SHELXL-2014.[53] Anisotropic thermal parameters were assigned to all non-hydrogen atoms. All aromatic hydrogen atoms of the abpt ligand were inserted in calculated positions appropriate for the data collection temperature (C–H = 0.95 Å) with the isotropic displacement parameters based on the parent C atom, $U_{iso}(H) = 1.2U_{eq}(C)$. Hydrogen atoms of the uncoordinated water molecule in **1** and coordinated solvent molecules in **2** and **3**, as well as amino-H atoms in all compounds, were found in the difference map and then refined using a riding model. An analysis of the hydrogen bonds was performed using SHELXL-2014, while PLATON[54] running under WinGX[55] was used to analyze the π–π interactions. DIAMOND[56] was used for molecular graphics. The crystal and experimental data are given in Tables S1–S5.†

Theoretical methods

The ORCA 4.0 computational package was used for all theoretical calculations.[44] The calculations of the ZFS parameters were done using the state-averaged complete active space self-consistent field (SA-CASSCF)[57] wave functions complemented by the N-electron valence second-order perturbation theory (NEVPT2)[58] using the triple-ζ basis set def2-TZVP[59] for all atoms. In the state-averaged approach, all multiplets for a given electron configuration were equally weighted. The ZFS parameters, based on dominant spin–orbit coupling contributions from excited states, were calculated through quasi-degenerate perturbation theory (QDPT),[60] in which an approximation to the Breit–Pauli form of the spin–orbit coupling operator (SOMF approximation)[61] and the effective Hamiltonian theory[62] were utilized. The calculations utilized the RIJCOSX approximation with the auxiliary Coulomb basis def2/JK.[63] Increased integration grids (Grid6 and GridX6 in the ORCA convention) and tight SCF convergence criteria were used in all calculations. The Mayer bond orders were calculated with the CAM-B3LYP functional[64] and the auxiliary def2/J basis set was also utilized[65] together with the RI-JK approximation to exact exchange as implemented in ORCA. The *ab initio* ligand field theory (AILFT) analysis was done for CAS(7,5) calculations as implemented in ORCA, which resulted in the Racah parameters (B and C), the spin–orbit coupling constant ξ, and the matrix elements of the ligand field matrix V^{LFT}. Subsequently a home-made program was used to fit the AOM parameters using the AOMX software by minimizing the difference of the V^{LFT} matrix elements between ORCA and AOMX. Here, the FORTRAN code PRAXIS was used to find the best solution.[66]

Conclusions

In conclusion, we report on the syntheses and characterization of six Co(II) mononuclear hexacoordinate complexes comprising the bidentate abpt ligand and various co-ligands in axial positions. Several linear and non-linear pseudohalides, such as NCSe (selenocyanate), $N\{C(CN)_2\}_2^-$ (1,1,3,3-tetracyano-2-azapropenide, tcap), $NO_2C(CN)_2^-$ (nitrodicyanomethanide, nodcm), $C(CN)\{C(CN)_2\}_2^-$ (1,1,2,3,3-pentacyanopropenide, pcp), NO_2NCN^- (nitrocyanamide, nca), and $ONC(CN)_2^-$ (nitrosodicyanomethanide, ndcm) were employed in the synthesis, but X-ray analysis confirmed only the coordination of the nca, NCSe, and ndcm anions in compounds **4–6**, whereas in the rest of the reported compounds **1–3**, the solvent molecules (H_2O or CH_3OH) were incorporated in the first coordination sphere. The magnetic measurements confirmed an S = 3/2 ground spin state with large magnetic anisotropy. The analyses of the experimental magnetic data supported by CASSCF/NEVPT2 calculations were based on either the spin Hamiltonian formalism (compounds **1–5**) or on the L–S Hamiltonian (compound **6**) and revealed significant energy separations of the lowest Kramers doublets, and thus large magnetic anisotropy. The ground state properties were also rationalized using AILFT together with the AOM, thus explaining the role of a small bite angle of the abpt equatorial ligands and variation of the ligand field strength of the respective axial co-ligands. The measurements of AC susceptibility substantiated the slow relaxation of the magnetization at a small static magnetic field with one relaxation process for all compounds **1–6**, thus classifying these substances as field-induced SMMs. The effective spin reversal energy barrier was evaluated by several approaches and a maximal $U_{eff} \approx 100$ K was found for compounds **1** and **2**.

Conflicts of interest

There are no conflicts to declare.

Open Access Article. Published on 19 December 2017. Downloaded on 9/21/2024 9:05:42 PM.
This article is licensed under a Creative Commons Attribution-NonCommercial 3.0 Unported Licence.

Acknowledgements

This work was financially supported by the Czech Science Foundation (Grant No. 17-08992S) and the National Program of Sustainability (NPU LO1305) of the Ministry of Education, Youth and Sports of Czech Republic. This work was also supported by the Slovak Research and Development Agency under contract No. APVV-14-0078 and by the project VEGA 1/0598/14.

Notes and references

1 N. Ishikawa, M. Sugita, T. Ishikawa, S.-y. Koshihara and Y. Kaizu, *J. Am. Chem. Soc.*, 2003, **125**, 8694–8695.
2 R. Sessoli, D. Gatteschi, A. Caneschi and M. A. Novak, *Nature*, 1993, **365**, 141–143.
3 (*a*) D. Gatteshi, R. Sessoli and J. Villain, *Molecular Nanomagnets*, Oxford University Press, New York, 2006; (*b*) Single Molecule Magnet and Related Phenomena, in *Structure and Bonding*, ed. R. Winpenny, Springer, Berlin, 2006, vol. 122.
4 J. S. Miller and D. Gatteschi, Molecule-based magnets themed issue No. 6, *Chem. Soc. Rev.*, 2011, **40**, 3065.
5 R. Boča, *Coord. Chem. Rev.*, 2004, **248**, 757–815.
6 A. K. Bar, C. Pichon and J.-P. Sutter, *Coord. Chem. Rev.*, 2016, **308**, 346–380.
7 (*a*) O. Waldmann, *Inorg. Chem.*, 2007, **46**, 10035–10037; (*b*) F. Neese and D. A. Pantazis, *Faraday Discuss.*, 2011, **148**, 229–238.
8 (*a*) J. M. Zadrozny, D. J. Xiao, J. R. Long, M. Atanasov, F. Neese, F. Grandjean and G. J. Long, *Inorg. Chem.*, 2013, **52**, 13123–13131; (*b*) J. M. Zadrozny, D. J. Xiao, M. Atanasov, G. J. Long, F. Grandjean, F. Neese and J. R. Long, *Nat. Chem.*, 2013, **5**, 577–581.
9 (*a*) J. M. Zadrozny, M. Atanasov, A. M. Bryan, C.-Y. Lin, B. D. Rekken, P. P. Power, F. Neese and J. R. Long, *Chem. Sci.*, 2013, **4**, 125–138; (*b*) C. Mathonière, H.-J. Lin, D. Siretanu, R. Clérac and J. M. Smith, *J. Am. Chem. Soc.*, 2013, **135**, 19083–19086; (*c*) X. Feng, C. Mathonière, I.-R. Jeon, M. Rouzières, A. Ozarowski, M. L. Aubrey, M. I. Gonzalez, R. Clérac and J. R. Long, *J. Am. Chem. Soc.*, 2013, **135**, 15880–15884; (*d*) W. H. Harman, T. D. Harris, D. E. Freedman, H. Fong, A. Chang, J. D. Rinehart, A. Ozarowski, M. T. Sougrati, F. Grandjean, G. J. Long, J. R. Long and C. J. Chang, *J. Am. Chem. Soc.*, 2010, **132**, 18115–18126; (*e*) D. E. Freedman, W. H. Harman, T. D. Harris, G. J. Long, C. J. Chang and J. R. Long, *J. Am. Chem. Soc.*, 2010, **132**, 1224–1225; (*f*) D. Weismann, Y. Sun, Y. Lan, G. Wolmershäuser, A. K. Powell and H. Sitzmann, *Chem. – Eur. J.*, 2011, **17**, 4700–4704.
10 S. Mossin, B. L. Tran, D. Adhikari, M. Pink, F. W. Heinemann, J. Sutter, R. K. Szilagyi, K. Meyer and D. J. Mindiola, *J. Am. Chem. Soc.*, 2012, **134**, 13651–13661.
11 (*a*) R. C. Poulten, M. J. Page, A. G. Algarra, J. J. Le Roy, I. López, E. Carter, A. Llobet, S. A. Macgregor, M. F. Mahon, D. M. Murphy, M. Murugesu and M. K. Whittlesey, *J. Am. Chem. Soc.*, 2013, **135**, 13640–13643; (*b*) W. Lin, T. Bodenstein, V. Mereacre, K. Fink and A. Eichhöfer, *Inorg. Chem.*, 2016, **55**, 2091–2100.
12 (*a*) J. Miklovič, D. Valigura, R. Boča and J. Titiš, *Dalton Trans.*, 2015, **44**, 12484–12487; (*b*) K. E. R. Marriott, L. Bhaskaran, C. Wilson, M. Medarde, S. T. Ochsenbein, S. Hill and M. Murrie, *Chem. Sci.*, 2015, **6**, 6823–6828; (*c*) D. Lomjanský, J. Moncol', C. Rajnák, J. Titiš and R. Boča, *Chem. Commun.*, 2017, **53**, 6930–6932.
13 R. Boča, C. Rajnák, J. Titiš and D. Valigura, *Inorg. Chem.*, 2017, **56**, 1478–1482.
14 (*a*) R. Ishikawa, R. Miyamoto, H. Nojiri, B. K. Breedlove and M. Yamashita, *Inorg. Chem.*, 2013, **52**, 8300–8302; (*b*) G. A. Craig, J. J. Marbey, S. Hill, O. Roubeau, S. Parsons and M. Murrie, *Inorg. Chem.*, 2014, **54**, 13–15; (*c*) J. Vallejo, A. Pascual-Álvarez, J. Cano, I. Castro, M. Julve, F. Lloret, J. Krzystek, G. De Munno, D. Armentano, W. Wernsdorfer, R. Ruiz-García and E. Pardo, *Angew. Chem., Int. Ed.*, 2013, **52**, 14075–14079.
15 T. Jurca, A. Farghal, P.-H. Lin, I. Korobkov, M. Murugesu and D. S. Richeson, *J. Am. Chem. Soc.*, 2011, **133**, 15814–15817.
16 See *e.g.*: (*a*) R. Boča, J. Miklovič and J. Titiš, *Inorg. Chem.*, 2014, **53**, 2367–2369; (*b*) D.-K. Cao, J.-Q. Feng, M. Ren, Y.-W. Gu, Y. Song and M. D. Ward, *Chem. Commun.*, 2013, **49**, 8863–8865; (*c*) J. M. Zadrozny, J. Liu, N. A. Piro, C. J. Chang, S. Hill and J. R. Long, *Chem. Commun.*, 2012, **48**, 3927–3929; (*d*) J. M. Zadrozny and J. R. Long, *J. Am. Chem. Soc.*, 2011, **133**, 20732–20734; (*e*) M. Idešicová and R. Boča, *Inorg. Chim. Acta*, 2013, **408**, 162–171; (*f*) M. Idešicová, Ľ. Dlháň, J. Moncoľ, J. Titiš and R. Boča, *Polyhedron*, 2012, **36**, 79–84; (*g*) M. Idešicová, J. Titiš, J. Krzystek and R. Boča, *Inorg. Chem.*, 2013, **52**, 9409–9417.
17 See *e.g.*: (*a*) N. Nedelko, A. Kornowicz, I. Justyniak, P. Aleshkevych, D. Prochowicz, P. Krupiński, O. Dorosh, A. Ślawska-Waniewska and J. Lewiński, *Inorg. Chem.*, 2014, **53**, 12870–12876; (*b*) R. Ruamps, L. J. Batchelor, R. Guillot, G. Zakhia, A.-L. Barra, W. Wernsdorfer, N. Guihery and T. Mallah, *Chem. Sci.*, 2014, **5**, 3418–3424; (*c*) D. M. Pinero Cruz, D. N. Woodruff, I.-R. Jeon, I. Bhowmick, M. Secu, E. A. Hillard, P. Dechambenoit and R. Clerac, *New J. Chem.*, 2014, **38**, 3443–3448; (*d*) C. Rajnák, J. Titiš, I. Šalitroš, R. Boča, O. Fuhr and M. Ruben, *Polyhedron*, 2013, **65**, 122–128.
18 (*a*) V. Chandrasekhar, A. Dey, A. J. Mota and E. Colacio, *Inorg. Chem.*, 2013, **52**, 4554–4561; (*b*) Y.-Y. Zhu, C. Cui, Y.-Q. Zhang, J.-H. Jia, X. Guo, C. Gao, K. Qian, S.-D. Jiang, B.-W. Wang, Z.-M. Wang and S. Gao, *Chem. Sci.*, 2013, **4**, 1802–1806; (*c*) J. Vallejo, I. Castro, R. Ruiz-García, J. Cano, M. Julve, F. Lloret, G. De Munno, W. Wernsdorfer and E. Pardo, *J. Am. Chem. Soc.*, 2012, **134**, 15704–15707.
19 (*a*) X.-C. Huang, C. Zhou, D. Shao and X.-Y. Wang, *Inorg. Chem.*, 2014, **53**, 12671–12673; (*b*) P. Antal, B. Drahoš, R. Herchel and Z. Trávníček, *Inorg. Chem.*, 2016, **55**, 5957–5972; (*c*) B. Drahoš, R. Herchel and Z. Trávníček, *Inorg. Chem.*, 2017, **56**, 5076–5088.

 This journal is © The Royal Society of Chemistry 2018

Open Access Article. Published on 19 December 2017. Downloaded on 9/21/2024 9:05:42 PM.
This article is licensed under a Creative Commons Attribution-NonCommercial 3.0 Unported Licence.

20 L. Chen, J. Wang, J.-M. Wei, W. Wernsdorfer, X.-T. Chen, Y.-Q. Zhang, Y. Song and Z.-L. Xue, *J. Am. Chem. Soc.*, 2014, **136**, 12213–12216.
21 Y. Y. Zhu, C. Cui, Y. Q. Zhang, J. H. Jia, X. Guo, C. Gao, K. Qian, S. D. Jiang, B. W. Wang, Z. M. Wang and S. Gao, *Chem. Sci.*, 2013, **4**, 1802–1806.
22 (*a*) V. V. Novikov, A. A. Pavlov, Y. V. Nelyubina, M.-E. Boulon, O. A. Varzatskii, Y. Z. Voloshin and R. E. P. Winpenny, *J. Am. Chem. Soc.*, 2015, **137**, 9792–9795; (*b*) A. A. Pavlov, Y. V. Nelyubina, S. V. Kats, L. V. Penkova, N. N. Efimov, A. O. Dmitrienko, A. V. Vologzhanina, A. S. Belov, Y. Z. Voloshin and V. V. Novikov, *J. Phys. Chem. Lett.*, 2016, **7**, 4111–4116.
23 R. Herchel, L. Váhovská, I. Potočňák and Z. Trávníček, *Inorg. Chem.*, 2014, **53**, 5896–5898.
24 (*a*) R. Herchel, Z. Trávníček and R. Zbořil, *Inorg. Chem.*, 2011, **50**, 12390–12392; (*b*) F. Setifi, C. Charles, S. Houille, F. Thétiot, S. Triki, C. J. Gómez-García and S. Pillet, *Polyhedron*, 2013, **61**, 242–247.
25 (*a*) N. S. Gill, R. H. Nuttall, D. E. Scarfe and D. W. A. Sharp, *J. Inorg. Nucl. Chem.*, 1961, **18**, 79–87; (*b*) R. J. H. Clark and C. S. Williams, *Inorg. Chem.*, 1965, **4**, 350–357.
26 M. Shakir, S. Parveen, N. Begum and Y. Azim, *Polyhedron*, 2003, **22**, 3181–3186.
27 (*a*) U. García-Couceiro, O. Castillo, J. Cepeda, A. Luque, S. Pérez-Yáñez and P. Román, *Inorg. Chim. Acta*, 2009, **362**, 4212–4218; (*b*) P. J. Kunkeler, P. J. van Koningsbruggen, J. P. Cornelissen, A. N. van der Horst, A. M. van der Kraan, A. L. Spek, J. G. Haasnoot and J. Reedijk, *J. Am. Chem. Soc.*, 1996, **118**, 2190–2197; (*c*) M. Shakir, S. Parveen, N. Begum and P. Chingsubam, *Transition Met. Chem.*, 2004, **29**, 196–199.
28 W. L. Jolly, *Modern Inorganic Chemistry*, McGraw-Hill, Inc., New York, 1991.
29 C.-F. Sheu, S.-M. Chen, S.-C. Wang, G.-H. Lee, Y.-H. Liu and Y. Wang, *Chem. Commun.*, 2009, 7512–7514.
30 N. Moliner, M. C. Muñoz, S. Létard, J.-F. Létard, X. Solans, R. Burriel, M. Castro, O. Kahn and J. A. Real, *Inorg. Chim. Acta*, 1999, **291**, 279–288.
31 G. Dupouy, M. Marchivie, S. Triki, J. Sala-Pala, J.-Y. Salaün, C. J. Gómez-García and P. Guionneau, *Inorg. Chem.*, 2008, **47**, 8921–8931.
32 N. Moliner, A. B. Gaspar, M. C. Muñoz, V. Niel, J. Cano and J. A. Real, *Inorg. Chem.*, 2001, **40**, 3986–3991.
33 M.-L. Tong, C.-G. Hong, L.-L. Zheng, M.-X. Peng, A. Gaita-Ariño and J. M. Clemente Juan, *Eur. J. Inorg. Chem.*, 2007, **2007**, 3710–3717.
34 M.-X. Peng, C.-G. Hong, C.-K. Tan, J.-C. Chen and M.-L. Tong, *J. Chem. Crystallogr.*, 2006, **36**, 703–707.
35 I. Potočňák and L. Váhovská, *Z. Kristallogr.*, 2014, **229**, 579–586.
36 A. B. Gaspar, M. Carmen Muñoz, N. Moliner, V. Ksenofontov, G. Levchenko, P. Gütlich and J. Antonio Real, *Monatsh. Chem.*, 2003, **134**, 285–294.
37 R. Boča, *Struct. Bonding*, 2006, **117**, 1–264.
38 J. Titiš and R. Boča, *Inorg. Chem.*, 2011, **50**, 11838–11845.
39 R. Boča, *Theoretical Foundations of Molecular Magnetism*, Elsevier, Amsterdam, 1999.
40 J. S. Griffith, *The theory of transition metal ions*, Cambridge University Press, 1961.
41 M. E. Lines, *Phys. Rev.*, 1963, **131**, 546–555.
42 B. N. Figgis, M. Gerloch, J. Lewis, F. E. Mabbs and G. A. Webb, *J. Chem. Soc. A*, 1968, 2086–2093.
43 R. Boča, *A Handbook of Magnetochemical Formulae*, Elsevier, Amsterdam, 2012.
44 (*a*) F. Neese, *Wiley Interdiscip. Rev.: Comput. Mol. Sci.*, 2012, **2**, 73–78; (*b*) F. Neese, *Wiley Interdiscip. Rev.: Comput. Mol. Sci.*, 2018, **8**, e1327.
45 K. Pierloot, *Computational Organometallic Chemistry*, ed. T. R. Cundari, Marcel Dekker, Inc., New York, 2001, p. 123.
46 (*a*) C. Schäffer, *Pure Appl. Chem.*, 1970, **24**, 361–392; (*b*) T. Schönherr, M. Atanasov and H. Adamsky, ed. J. A. McCleverty and T. J. Meyer, *Comprehensive Coordination Chemistry II, From Biology to Nanotechnology*, Elsevier, 2003, vol. 2, pp. 443–455; (*c*) B. N. Figgis and M. A. Hitchman, *Ligand Field Theory and Its Applications*, Wiley-VCH, New York, 2000.
47 (*a*) M. Atanasov, D. Ganyushin, K. Sivalingam and F. Neese, in *Molecular Electronic Structures of Transition Metal Complexes II*, ed. D. M. P. Mingos, P. Day and J. P. Dahl, Springer Berlin Heidelberg, Berlin, Heidelberg, 2012, pp. 149–220; (*b*) S. K. Singh, J. Eng, M. Atanasov and F. Neese, *Coord. Chem. Rev.*, 2017, **344**, 2–25.
48 P. E. Hoggard, *Topics in Current Chemistry*, Springer-Verlag, Heinrich Heine Universitat, Berlin, Germany, 1994, vol. 171, pp. 113–141. The AOMX program is maintained by H. Adamsky, Institut fur Theoretische Chemie, Berlin, Germany, Springer-Verlag, Heinrich Heine Universitat, e-mail: adamsky@theochem.uni-duesseldorf.de.
49 See *e.g.*: (*a*) I. Nemec, R. Herchel and Z. Trávníček, *Dalton Trans.*, 2016, **45**, 12479–12482; (*b*) C. Rajnák, J. Titiš, O. Fuhr, M. Ruben and R. Boča, *Inorg. Chem.*, 2014, **53**, 8200–8202; (*c*) D. Valigura, C. Rajnak, J. Moncol, J. Titis and R. Boca, *Dalton Trans.*, 2017, **46**, 10950–10956.
50 R. L. Carlin, *Magnetochemistry*, Springer-Verlag, Berlin, 1986.
51 *Oxford Diffraction, CrysAlis CCD, CCD Data Collection GUI*, Oxford Diffraction Ltd., Oxford, UK, 2007.
52 L. Palatinus and G. J. Chapuis, *Appl. Crystallogr.*, 2007, **40**, 786–790.
53 G. M. Sheldrick, *Acta Crystallogr., Sect. C: Struct. Chem.*, 2017, **71**, 3–8.
54 A. L. Spek, *Acta Crystallogr., Sect. D: Biol. Crystallogr.*, 2009, **65**, 148–155.
55 L. J. Farrugia, *J. Appl. Crystallogr.*, 1999, **32**, 837–838.
56 K. Brandenburg, *DIAMOND (Version 3.2i) Crystal Impact GbR*, Bonn, Germany, 2009.
57 P. Å. Malmqvist and B. O. Roos, *Chem. Phys. Lett.*, 1989, **155**, 189–194.
58 (*a*) C. Angeli, R. Cimiraglia and J.-P. Malrieu, *Chem. Phys. Lett.*, 2001, **350**, 297–305; (*b*) C. Angeli, R. Cimiraglia, S. Evangelisti, T. Leininger and J.-P. Malrieu, *J. Chem. Phys.*, 2001, **114**, 10252–10264; (*c*) C. Angeli, R. Cimiraglia and J.-P. Malrieu, *J. Chem. Phys.*, 2002, **117**, 9138–9153.

Open Access Article. Published on 19 December 2017. Downloaded on 9/21/2024 9:05:42 PM.
This article is licensed under a Creative Commons Attribution-NonCommercial 3.0 Unported Licence.

59 F. Weigend and R. Ahlrichs, *Phys. Chem. Chem. Phys.*, 2005, **7**, 3297–3305.
60 D. Ganyushin and F. Neese, *J. Chem. Phys.*, 2006, **125**, 024103.
61 F. Neese, *J. Chem. Phys.*, 2005, **122**, 034107.
62 R. Maurice, R. Bastardis, C. de Graaf, N. Suaud, T. Mallah and N. Guihéry, *J. Chem. Theory Comput.*, 2009, **5**, 2977–2984.
63 F. Weigend, *J. Comput. Chem.*, 2008, **29**, 167–175.
64 T. Yanai, D. P. Tew and N. C. Handy, *Chem. Phys. Lett.*, 2004, **393**, 51–57.
65 F. Weigend, *Phys. Chem. Chem. Phys.*, 2006, **8**, 1057–1065.
66 R. Brent, *Algorithms for Minimization without Derivatives*, Dover, 2002.

This journal is © The Royal Society of Chemistry 2018